Review

Shiwei Tang, Qiong He, Shiyi Xiao, Xueqin Huang and Lei Zhou*

Fractal plasmonic metamaterials: physics and applications

Abstract: We review our recent works on a particular type of metamaterials (MTMs), which are metallic plates drilled with periodic arrays of subwavelength apertures typically in fractal-like complex shapes. We first show that such MTMs can well mimic plasmonic metals in terms of surface plasmon properties, but with plasmon resonances solely dictated by their aperture geometries rather than the constitutional materials. We then develop an effective-medium description for such plasmonic MTMs based on the mode expansion theory. Based on these theoretical understandings, we show that such MTMs exhibit several interesting applications, such as superlensing, hyperlensing, and enhancing light-matter interactions, which are demonstrated by microwave experiments or full-wave simulations.

Keywords: light-matter interaction; metamaterials; mode expansion; surface plasmon.

DOI 10.1515/ntrev-2014-0025
Received September 4, 2014; accepted March 26, 2015; previously published online May 22, 2015

1 Introduction

Controlling electromagnetic (EM) waves at will has always been fascinating, but conventional materials exhibit limited abilities in achieving this aim. Metamaterials (MTMs) have recently attracted widespread interest due to their extraordinary physical properties and potential applications. MTMs are artificial EM materials composed of subwavelength local resonant structures of electric and/or magnetic type, and thus, they can possess arbitrary values of permittivity ε and permeability μ dictated by the resonant structures. Many exciting new physical phenomena were predicted or demonstrated with MTMs, such as negative refraction [1, 2], superlensing [3], optical magnetism [4–12], invisible cloaking [13, 14], subwavelength cavities [15], and so on.

Recently, much attention was paid to the plasmonic properties of MTMs, partially related to the discovery of extraordinary optical transmission (EOT) on a Ag film drilled with subwavelength hole array [16]. It was soon understood that the EOT is achieved by exciting the surface plasmon polaritons (SPPs) on the Ag film aided by Bragg scatterings. Subsequently, many SPP-related studies were performed in connection to two important characteristics of SPP, i.e., significantly enlarged parallel wave vector and local field [17–20]. With these two attractive properties, one naturally expects that SPP can help achieve subwavelength imaging and enhance light-matter interactions (LMI).

However, the plasmon frequency ω_p of a natural material is fixed by its electron density, which limits the applications in practice significantly. In 2004, Pendry et al. [18] demonstrated that a metallic plate with periodic square holes can mimic a plasmonic material in terms of SPP properties, with effective ω_p dictated by the structure rather than the constitutional materials. This opens up the road to realize engineered SPPs in structured systems at frequencies where natural materials do not support SPP resonances. Unfortunately, to make the idea work, one has to fill the holes with high-index materials [17, 18], which is not easy to realize in practice, particularly at higher frequencies.

In recent several years, motivated by an early series of studies on MTMs constructed by metallic planar fractals, we proposed a new type of MTMs that can overcome the above-mentioned difficulty. Instead of using hole arrays with simple shapes, here our MTMs are metallic plates drilled with fractal-like hole array. Although such fractal MTMs also exhibit interesting multiband EM responses

***Corresponding author: Lei Zhou,** State Key Laboratory of Surface Physics and Key Laboratory of Micro and Nano Photonic Structures (Ministry of Education), Fudan University, Shanghai 200433, China, e-mail: phzhou@fudan.edu.cn; and Collaborative Innovation Center of Advanced Microstructures, Fudan University, Shanghai 200433, China
Shiwei Tang, Qiong He, Shiyi Xiao and Xueqin Huang: State Key Laboratory of Surface Physics and Key Laboratory of Micro and Nano Photonic Structures (Ministry of Education), Fudan University, Shanghai 200433, China; and Collaborative Innovation Center of Advanced Microstructures, Fudan University, Shanghai 200433, China

[21, 22], here we only focus on the deep-subwavelength characteristics of a fractal pattern. We found that, without using high-index insertions, such fractal-based MTMs exhibit very peculiar SPP properties, making them ideal candidates to realize the SPP-related applications. In this paper, we briefly review our efforts in studying the fundamental physical properties of such MTMs and use them to realize certain applications. In this review, we only present the experimental realizations of the concept in the microwave regime. We note that full-wave simulations revealed that similar ideas can also be realized at high frequencies (i.e., terahertz to near infrared) upon downscaling the fractal size appropriately [23]. This review is organized as follows. We first introduce the basic concept and key properties of our plasmonic MTMs in Section 2. Section 3 is devoted to presenting an effective medium description of our plasmonic MTMs, based on which many interesting properties of the system can be understood in a simple way. We then demonstrate several typical applications of our plasmonic MTMs, mainly along the line of imaging-related applications (e.g., superlensing and hyperlensing effects) in Section 4 and LMI enhancement-related ones (e.g., slow-wave, perfect absorption, nonlinear generation, etc.) in Section 5. We conclude this review in Section 6.

2 Key properties of the plasmonic MTM

We first discuss the key SPP properties of our designed plasmonic MTMs [23]. Figure 1 illustrate a typical example of our structure – a 0.5-μm-thick silver film caved with four-level fractal slits arranged periodically with a lattice constant a=1 μm. Taking the dielectric constant of silver as $\varepsilon_{Ag}=5-f_p^2/f(f+if_r)$ with f_p=2175 THz and f_r=4.35 THz, we performed extensively finite-difference-time-domain (FDTD) simulations to study the SPP dispersions of the designed structure. The FDTD-calculated SPP dispersion relations are shown in Figure 2A and B. It is clear that two SPP bands exist on such structure surfaces, which bend drastically while approaching two frequencies (f_{p1}=41 THz and f_{p2}=78.7 THz, denoted by two dashed lines). We can identify the polarization of the SPP bands with the attenuated total reflection technique. With k_x fixed as π/a, we shine evanescent waves with different polarizations on the structure, and depicted in Figure 2C, the transmission spectra for $\vec{E}||\hat{x}$ (red circles) and $\vec{E}||\hat{y}$ (blue line) polarizations. By comparing panels A and C of Figure 2, we found that the lower SPP band in Figure 2A is apparently transverse-magnetic (TM)-like, since a TM-polarized evanescent wave can excite this mode but a transverse-electric (TE) one cannot. Similarly, we identified polarizations of all SPP bands and then label them correspondingly on the figure.

Compared with other plasmonic MTMs with simple-shaped apertures, our structure exhibits a crucial advantage – it can support simultaneously TM- and TE-like SPPs related to each resonance. Obviously, a metallic plate with square/circular holes cannot support SPPs without interesting high-index materials, since the shape resonances of such apertures are not enough deep-subwavelength. We also studied a metal plate with narrow rectangular holes [24]. While such structure can support a single TM-like SPP band traveling along the x direction (inset to Figure 2A), the SPP band for such system along the y direction cannot be formed since the subwavelength condition in this direction is not satisfied [17, 18]. In contrast, our fractal pattern is subwavelength along all directions and possesses multiple resonances, so that for each

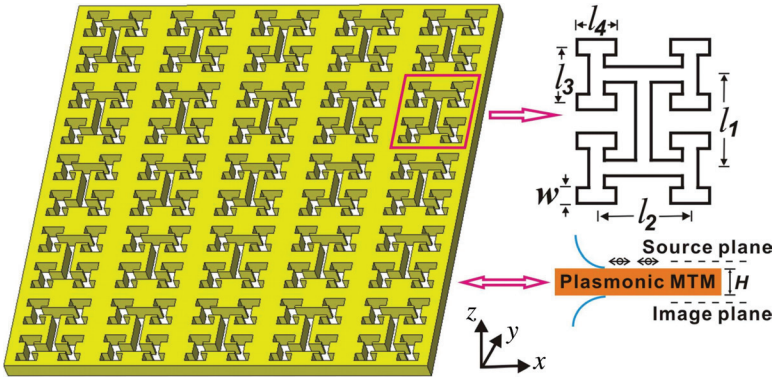

Figure 1: Geometry of the fractal MTM.
Unit cell structure: l_1=l_2=0.5 μm, l_3=l_4=0.25 μm, w=0.06 μm, H=0.5 μm. Reproduced from Ref. [23] with permission.

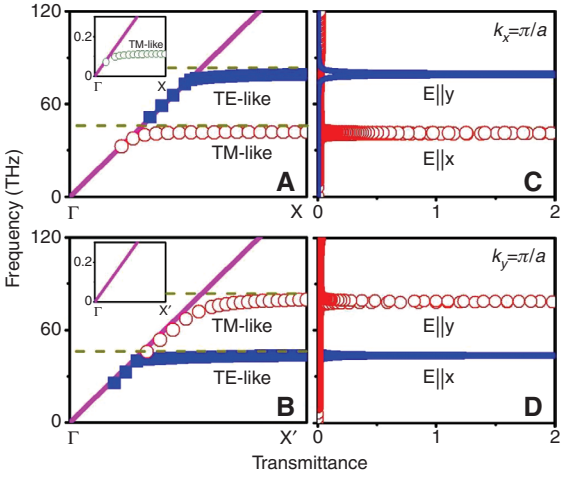

Figure 2: SPP band structures and transmission spectra of the fractal plate.
SPP band structures of the fractal plate calculated by FDTD simulations for (A) Γ→X and (B) Γ→X′ directions. Under the conditions of (C) $k_x=\pi/a$ and (D) $k_y=\pi/a$, FDTD calculated the transmission spectra under incident plane evanescent waves with different polarizations. Insets: SPP band structures of rectangle hole plate calculated by FDTD simulations, with structural details d=1 μm, s=4.2d, a=0.3d, and L=0.5d. Reproduced from [23] with permission.

resonance, SPP bands along both x and y directions can be formed (see Figure 2).

Another advantage of our system is that the plasmon frequency is closely related to the fractal geometry but is rather insensitive to the structure thickness. Taking three- and four-level fractals as examples, we depicted in Figure 3 that the plasmon resonance wavelength λ_p of the MTM can be efficiently changed by varying the slit line width w and scaling the structure. Therefore, we can, in principle, design a plasmonic MTM at any desired frequency according to realistic application requests.

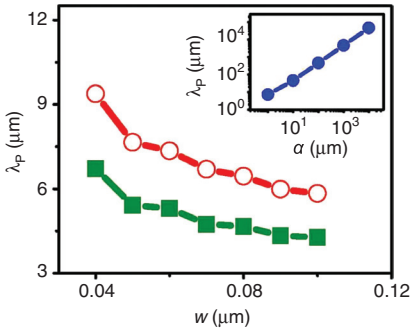

Figure 3: FDTD-calculated plasmon wavelength λ_p as functions of the slit width w when using three- (solid squares) and four-level fractals (open circles).
Inset shows the calculated λ_p as a function of the periodicity a of the fractal array. Reproduced from [23] with permission.

In addition to the SPP properties discussed above, our MTM also possess very peculiar transmission/reflection properties. We have employed the FDTD method to study the properties of the transfer functions $[T^{TE}(k_{||}), T^{TM}(k_{||})]$ for the designed fractal lens. For propagating components (i.e., $k_{||}<k_0$), we found through FDTD simulations that the fractal structure supports high transmissions $T(k_{||})\approx1$ at the working frequency. More importantly, there is nearly no phase change for the transmitted waves under all incident angles and polarizations, as shown in Figure 4 by open stars. Therefore, information of all propagating components can be well transmitted through the fractal lens, without any distortions. In contrast, when the fractal lens is replaced by air, the phase change of transmitted wave strongly depends on the incidence angle, as shown in Figure 4 by solid circles.

3 Effective medium description of the plasmonic MTM

To understand the fascinating physical properties of our plasmonic MTMs in a simple way, in this section, we will establish an effective medium description for such systems [25]. Figure 5A shows the generic system that we consider, where the plasmonic MTM occupies a semi-infinite space. For simplicity, here we only consider the microwave frequency domain so that metallic can be treated as a perfect electric conductor (PEC). The aperture can take any symmetrical complex shape as long as the resonance wavelength associated with it is much longer than its own size (i.e., $\lambda \gg d$) and is arranged in a square lattice with periodicity d. We first extend a previously established effective medium theory (EMT) for simple-shaped aperture case

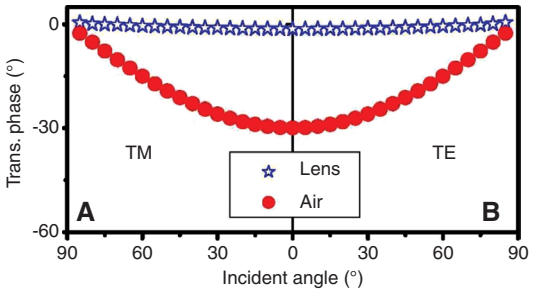

Figure 4: Phase change of the transmitted wave through fractal lens and air layer.
FDTD-calculated phase change of the transmitted wave through our fractal lens (blue stars) and an air layer of the same thickness (red circles) as functions of the incident angle for TM- (A) and TE-polarized (B) incident waves. The working frequency is 41 THz. Reproduced from [23] with permission.

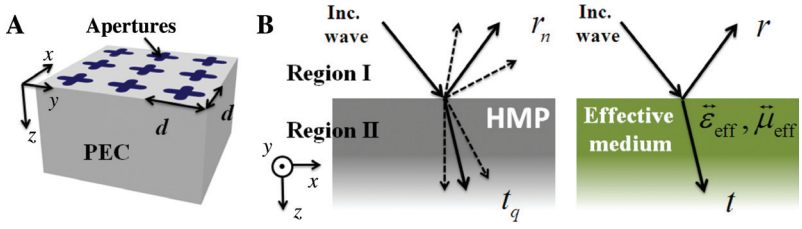

Figure 5: Geometry of MTM and scheme of mapping.
(A) Geometry of a plasmonic MTM. (B) Scheme of mapping a plasmonic MTM to a homogeneous anisotropic effective medium. Reproduced from [25] with permission.

[17] to a general situation. Symmetry argument tells us that the effective permittivity/permeability tensor of the MTM should be

$$\ddot{\varepsilon}_{\text{eff}}=\varepsilon_0\begin{pmatrix}\varepsilon_{\text{eff}}^{\parallel} & 0 & 0\\ 0 & \varepsilon_{\text{eff}}^{\parallel} & 0\\ 0 & 0 & \varepsilon_{\text{eff}}^{\perp}\end{pmatrix}, \ddot{\mu}_{\text{eff}}=\mu_0\begin{pmatrix}\mu_{\text{eff}}^{\parallel} & 0 & 0\\ 0 & \mu_{\text{eff}}^{\parallel} & 0\\ 0 & 0 & \mu_{\text{eff}}^{\perp}\end{pmatrix} \tag{1}$$

In what follows, we determined the four unknowns $(\varepsilon_{\text{eff}}^{\parallel}, \varepsilon_{\text{eff}}^{\perp}, \mu_{\text{eff}}^{\parallel}, \mu_{\text{eff}}^{\perp})$ by requesting that the two systems (e.g., model and the realistic one) exhibit the same optical responses with respect to general excitations (see Figure 5B), under certain approximations.

Suppose that the realistic system is illuminated by a TE-polarized light with a parallel wave vector $k_{\parallel}^0\hat{x}$. The scattering properties of such a system can be solved by the standard mode expansion method [17, 26, 27]. We retain only the fundamental modes in both regions (i.e., the specular reflection in region I and the fundamental waveguide mode inside the aperture) but neglect all the high-order modes. This single-mode approximation is widely used and is physically sound here since we assume $\lambda \gg d$ so that all high-order modes are evanescent waves. Under this approximation, we found that the specular reflection coefficient is written as

$$r_0=\frac{|S_0|^2 k_z^{\text{air}}/k_z^{\text{WG}}-1}{|S_0|^2 k_z^{\text{air}}/k_z^{\text{WG}}-1} \tag{2}$$

where

$$|S_0|^2=\frac{\left|\int_{\text{u.c.}}(\vec{E}_{\parallel}^{\text{in}})^*(\vec{E}_{0,\parallel}^{\text{WG}})\,d\vec{r}_{\parallel}\right|^2}{\int_{\text{u.c.}}\left|\vec{E}_{\parallel}^{\text{in}}\right|^2 d\vec{r}_{\parallel}\int_{\text{u.c.}}\left|\vec{E}_{0,\parallel}^{\text{WG}}\right|^2 d\vec{r}_{\parallel}} \tag{3}$$

represents the overlapping between the incident plane wave $\vec{E}_{\parallel}^{\text{in}}$ and the fundamental waveguide mode $\vec{E}_{0,\parallel}^{\text{WG}}$. Here, only the parallel field components are relevant, and the integrals are performed within a unit cell. $k_z^{\text{air}}, k_z^{\text{WG}}$ are the z-components of k vectors of waves in different regions. Explicitly,

$$k_z^{\text{WG}}=\sqrt{\varepsilon_h}\sqrt{\omega^2-\omega_c^2}/c \tag{4}$$

where ε_h is the relative permittivity of the medium filling the aperture and ω_c is the cutoff frequency of the fundamental waveguide mode, obtainable by numerical simulations for general aperture cases.

In principle, S_0 depends on the incident angle. However, such angular dependence is very weak here since the variation of incident field across the aperture area is weak when the aperture is deep-subwavelength in size. Therefore, we adopt the second approximation to neglect such angular dependence and assume that S_0 can be calculated under normal incidence condition. For rectangle-shaped aperture, we get from Eq. (3) that $S_0=2\sqrt{2}a/\pi d$ [26]. In general, complex-shaped apertures, S_0 can be easily calculated by numerical simulations after $\vec{E}_{0,\parallel}^{\text{WG}}$ has been solved.

We now derive the effective-medium parameters of the structure. Under exactly the same external illumination, we find that the reflection coefficient of the model system (i.e., the anisotropic MTM) is

$$r=\frac{\mu_{\text{eff}}^{\parallel}k_z^{\text{air}}/k_z^{\text{MTM}}-1}{\mu_{\text{eff}}^{\parallel}k_z^{\text{air}}/k_z^{\text{MTM}}-1}, \tag{5}$$

where

$$k_z^{\text{MTM}}=\sqrt{(\omega/c)^2\varepsilon_{\text{eff}}^{\parallel}\mu_{\text{eff}}^{\parallel}-k_{\parallel}^2\mu_{\text{eff}}^{\parallel}/\mu_{\text{eff}}^{\perp}} \tag{6}$$

is the z component of the k vector for a TE-polarized wave traveling inside such an anisotropic MTM. Comparing Eqs. (5) and (6) with Eqs. (2)–(4), we get

$$\begin{cases}\varepsilon_{\text{eff}}^{\parallel}=(1-\omega_c^2/\omega^2)\varepsilon_h/|S_0|^2\\ \mu_{\text{eff}}^{\parallel}=|S_0|^2\\ \mu_{\text{eff}}^{\perp}=\infty\end{cases}. \tag{7}$$

We can get the values of $\varepsilon_{\text{eff}}^{\parallel}, \varepsilon_{\text{eff}}^{\perp}, \mu_{\text{eff}}^{\parallel}$ with similar calculations for TM-polarized excitations. For $\varepsilon_{\text{eff}}^{\parallel}, \mu_{\text{eff}}^{\parallel}$, the TM calculations yield the same expressions as recorded in Eq. (7), which justified our TE calculations independently.

Meanwhile, we get additionally from the TM calculations that

$$\varepsilon_{\text{eff}}^{\perp}=\infty. \tag{8}$$

Eqs. (7) and (8) are the general EMT description of the plasmonic MTM, valid for any frequency satisfying the subwavelength condition $\lambda \gg d$. There is a particularly important and interesting case when we set the working frequency as the waveguide cutoff ($\omega=\omega_c$). In that case, we find that

$$\ddot{\varepsilon}_{\text{eff}}=\varepsilon_0\begin{pmatrix}0&0&0\\0&0&0\\0&0&\infty\end{pmatrix}, \ddot{\mu}_{\text{eff}}=\mu_0\begin{pmatrix}|S_0|^2&0&0\\0&|S_0|^2&0\\0&0&\infty\end{pmatrix}. \tag{9}$$

If we can design a plasmonic MTM exhibiting $|S_0|^2\to 0$, Eq. (9) tells us that such a system (at the frequency $\omega=\omega_c$) can well mimic a particular transformation-optics (TO) medium –"optic-null medium" (ONM) [25] described by

$$\ddot{\varepsilon}_{\text{ONM}}=\ddot{\mu}_{\text{ONM}}=\begin{pmatrix}0&0&0\\0&0&0\\0&0&\infty\end{pmatrix}. \tag{10}$$

The ONM, presenting an optically non-existing space and generated by a space stretch operation, exhibits very interesting optical properties. As shown in Figure 6, the ONM allows prefect transmissions for propagating and evanescent waves with arbitrary polarizations and incident angles without any phase accumulations. We emphasize that an ONM is fundamentally different from ε-near-zero materials [28–30] and isotropic zero-index-materials (ZIM) [31, 32]. Such an amazing property has been realized by our plasmonic MTM at the working frequency (see Figure 4), which confirms the validity of the EMT description from another viewpoint.

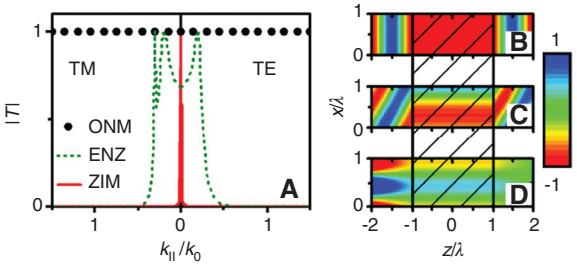

Figure 6: Transmission amplitudes and electric field distribution. (A) FEM-computed transmission amplitudes $|T|$ for EM waves with different incident angles and polarizations passing through a 2λ-thick slab of ONM (solid circles), ENZ (green dash line, with $\varepsilon=0.1$), or ZIM (red line), correspondingly. (B)–(D) FEM-simulated electric field (E_y) distributions for TE-polarized EM waves passing through a 2λ-thick ONM slab with parallel wave vectors: (B) $k_x=0$, (C) $k_x=0.5k_0$, (D) $k_x=1.2k_0$. Here, k_0 wave vector in vacuum and the shadow areas represent the ONM. Reproduced from [25] with permission.

4 Applications of the MTMs: imaging

After introducing the key properties and the effective medium description of the MTMs, we now demonstrate some typical applications of the systems. As we have discussed in the introduction, we will follow two logical lines to introduce the key applications of the system, namely the imaging- and LIM-enhancement-related applications. This section will focus on the imaging-related applications.

4.1 Superlens

As discussed above, our plasmonic MTM can well mimic an ONM at the working frequency. One of the most amazing properties of an ONM is that it can work as a superlens since it can transfer all the wave information across it without any distortions. To demonstrate that our MTM can indeed work as a superlens [23], we designed a microwave plasmonic MTM with unit-cell shown schematically in the right panel of Figure 7A. We put a dipole antenna on the source plane 1 mm above the lenses and placed a receiver dipole antenna on an image plane 1 mm below the lenses to measure the field distributions of the images. Both antennas are polarized along the y direction, connected to a vector network analyzer, and working at f=2.52 GHz coinciding with the plasmon frequency of the designed lenses for y polarization. When the source antenna is put at the unit cell center, the images formed by two lenses with thicknesses H=31.5 mm and H=63 mm are depicted in Figure 7B and C as open circles, which are in excellent agreement with the corresponding FDTD simulations (solid lines). Both measurements and FDTD results show that the images focused by our lenses are only ~8 mm wide, which are ~λ/15 recalling λ=119 mm. In contrast, the images formed without lenses (solid squares) do not show any subwavelength resolutions at all. In addition, the field strength is enhanced when a lens is added, and the working frequencies for two thickness cases remain at 2.53 GHz.

4.2 Radiation cancellation effect

Since the ONM represents an "optically" non-existing space, if we put a source on top of a slab, then the source will behave like that it is virtually placed on the exit plane of the ONM. We can experimentally demonstrate this point

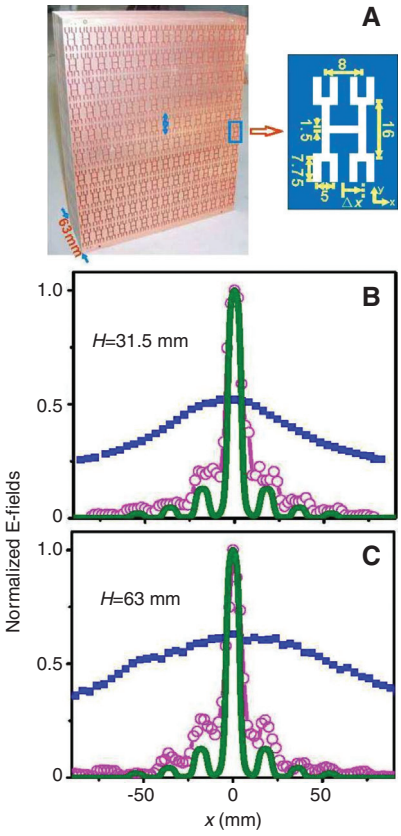

Figure 7: Picture of MTM and electric field distributions along the line perpendicular to the antenna.
(A) Picture of a 63-mm-thick fractal MTM and its unit cell structure (all lengths are measured in millimeters). Here the periodicity is 18 mm (32 mm) in $x(y)$ direction. (B) and (C) Electric field distributions along the line perpendicular to the antenna on the image plane obtained by experiments (open circles) and FDTD simulations (solid lines) for different lens thickness, referenced by the experimental results measured without any lens (solid squares). Here, the maximum electric field is normalized to 1 in the presence of a lens. Reproduced from [23] with permission.

[25]. As shown in the inset to Figure 8B, suppose we place a dipole antenna (length=16.5 mm) on top of an ONM slab with thickness h and in turn put on a PEC substrate. Since an ONM represents "optically" nothing, it appears that the dipole antenna is placed directly on top of the PEC. Thus, the dipole antenna cannot radiate, at all due to image cancellation effect, so that its return loss should approach to 1 (i.e., $|S_{11}|=1$). Varying the thickness h of the HMP slab, we found that the measured $|S_{11}|$ (open squares) of the antenna remains essentially at ~1. FDTD simulations performed on the realistic systems (red line) are in good agreement with the experimental results, which unambiguously demonstrated the "radiation cancellation" effect as predicted. We next performed a series of control experiments by replacing the HMP slabs by air gaps with the same thicknesses. The measured $|S_{11}|$ (green triangles) varies continuously from 1 to 0 as h increases from 3 to 30 mm, which is in perfect agreement with FDTD simulations (green line). Such an effect is expected since the cancellation of the dipole with its image is affected by the propagating phase inside the air gap, and thus, the cancellation is good only when $h\rightarrow 0$. As a final test, as we removed the PEC substrate, we found that the return loss of the antenna is nearly zero as if the slabs do not exist, again in good agreement with FDTD simulations as well as the expectations based on the ONM.

4.3 Hyperlens

The space-stretch operation can be applied not only to a Cartesian coordinate system but also to a cylindrical coordinate system. In the latter case, the resulting TO medium should be a cylindrical version of ONM, with EM parameters given by [33]

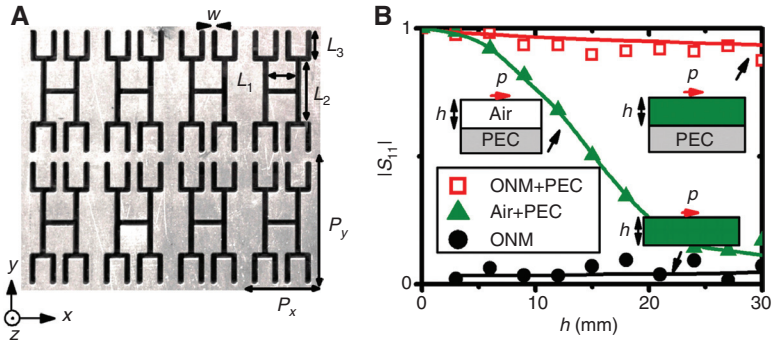

Figure 8: Picture of the fabricated MTM and return loss spectra.
(A) Picture of the fabricated sample with parameters L_1=12 mm, L_2=13 mm, L_3=6 mm, P_x=18 mm, P_y=31 mm, w=1 mm. (B) Return loss ($|S_{11}|$) spectra of a dipole antenna put on top of standing-alone ONM slabs (black), ONM slabs backed by a PEC substrate (red), and air gaps backed by a PEC substrate (green), obtained by experiment (symbols) and FDTD simulations (lines). Here, the working frequency is 2.63 GHz. Reproduced from [25] with permission.

$$\vec{\varepsilon}=\vec{\mu}=\begin{pmatrix}\infty & 0 & 0\\ 0 & 0 & 0\\ 0 & 0 & 0\end{pmatrix} \tag{11}$$

One of the most amazing applications of the cylindrical ONM is that it can work as a hyperlens, in the sense that it can not only form a subwavelength image but can also magnify the image so that a near-field information can be transferred to the far field. In this subsection, we perform FDTD simulations and microwave experiments to demonstrate this particular application [33].

The working principle is shown in Figure 9C. To fabricate the cylindrical ONM, we cut a 65-mm-thick plasmonic MTM slab into 18-mm-wide stripes (each containing 7 unit elements) and then arrange them into a cylindrical shape. We put two line sources on the inner surface of a cylindrical-shaped ONM layer and one monopole antenna on the outer surface of our sample to measure the field distribution. The inner and outer radii of the realized sample are 235 and 300 mm, respectively, and samples with other radii can be easily fabricated. Figure 9D depicts the calculated field distribution on the central *xy* plane of the realistic sample, which is in excellent agreement with the field distribution of the ideal cylindrical ONM (Figure 9C).

In our experiments, we used two identical monopole antennas (length=8 mm) as the source and another identical one as the probe. The two source antennas are fed with equal amplitude signals with a particular phase difference $\delta\varphi$ controlled by a phase shifter. With the working frequency still set at 2.63 GHz, we placed two monopoles on the inner surface of the device, separated by a distance of 18 mm (~$\lambda/6$) and then measured the field distribution on the image plane (exit surface of the hyperlens). As important references, we first measured the field distributions formed on the image plane when the hyperlens was removed, and we note that the two sources cannot be distinguished on the image planes (solid circles in Figure 10A and C). We next studied the cases when the hyperlens was added. From the measured distributions shown as solid circles in Figure 10A and C, we found that now the two monopoles can be clearly distinguished on the image plane, with measured half maximum width of each peak being roughly 20 mm ~$\lambda/6$. More importantly, now the separation of two peaks is 23 mm, which is enhanced by a factor of ~1.3 as compared to the original value 18 mm, and the field at the image peak is enhanced significantly (more than 7 times) than that without the hyperlens. All the experiments are consistent with theoretical expectation.

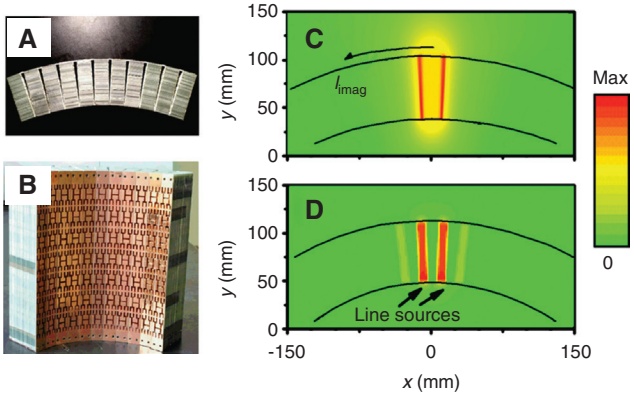

Figure 9: Pictures of the experiment sample and electric distributions for the hyperlensing effect.
(A) Top- and (B) side-view pictures of the experiment sample. $|E/E_{ref}|$ distributions for the hyperlensing effect realized by (C) a cylindrical ONM with parameter given by Eq. (10) and (D) our designed sample obtained by FDTD simulations at frequency 2.63 GHz. Reproduced from [25] with permission.

5 Applications of the MTMs: enhancement of LMI

We now describe another series of applications of our plasmonic MTMs, namely how to use them to enhance LMI.

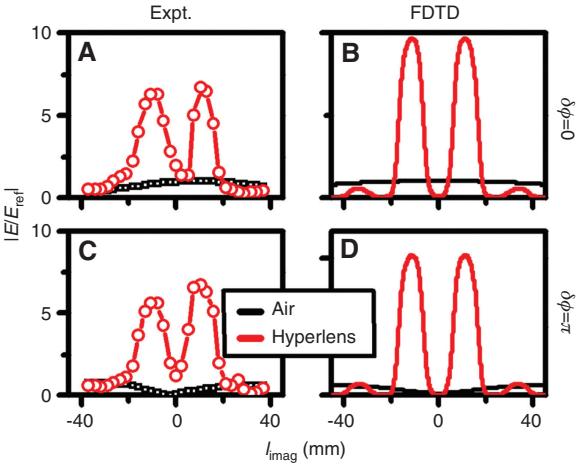

Figure 10: Electric field distributions at the outer surface of the hyperlens.
(A, C) Measured and (B, D) simulated $|E/E_{ref}|$ distributions at the outer surface of the hyperlens when two dipole antennas are placed on the inner surface of the hyperlens, fed by in phase (A and B) and out-of-phase (C and D) signals. Black lines/symbols correspond to the case of replacing the sample by air. In both measurements and simulations, the $|E|$ value at the position l_{imag}=0 mm in the in-phase case is taken as the reference $|E_{ref}|$. Reproduced from [25] with permission.

5.1 Enhancement of the non-linear optical effects

Optical bistability is a non-linear optical phenomenon that has many potential applications in optoelectronics. Conventional optical bistability devices consist of Fabry-Perot (FP) resonators filled with non-linear media [34–36]. To be able to sustain proper FP modes to provide the necessary feedback mechanism that amplifies the input signal, the optical thicknesses of the resonator must be at least of the order of the operating wavelength or the input signal must be prohibitively strong [37]. Such constraints severely limit the application and the integration of optical bistable devices. Here, we show that such constraint can be relieved with the help of our plasmonic MTMs. In particular, we present a realistic design working at 0.2 THz and show by FDTD simulations that optical bistability can occur in such a device with an excitation power 3500 times lower than the case of using an FP resonator of the same thickness. In addition, the bistability threshold field is essentially independent of film thickness, so that the device can be ultra-thin.

Figure 11A shows a unit cell of our device, which is a 60-μm-thick metallic plate (yellow region) perforated with a subwavelegth aperture with a symmetrical and interconnected lateral pattern (blue region). The aperture is embedded with non-linear material with permittivity ε_d. Figure 11B shows the FDTD-calculated transmission spectra of the device with varying ε_d. Note that the optical properties of the device are polarization-independent as the structure has a fourfold rotational symmetry on the *xy* plane. Remarkably, we find that the structure exhibits a perfect transmission peak at certain frequency, which is red-shifted when ε_d increases. Such a transparency is induced by the excitation of spoof SPs in the subwavelength structured metallic systems [17, 39–42].

Figure 12 plots the FDTD-calculated bistable hysteresis of devices with varying thickness *h* and line width *w*, operating at a frequency f=0.2 THz. The permittivity of the Kerr medium is $\varepsilon_d=2.25+\chi^{(3)}|E|^2$, with $\chi^{(3)}=1\times10^{-18}$ m^2/V^2, which is typical in semiconductors [44, 45]. The obtained results indicate that the bistability can occur for a device with thickness of 60 μm (Figure 12A), that is 1/25 of the operating wavelength; also, the bistability threshold field is essentially independent of the film thickness

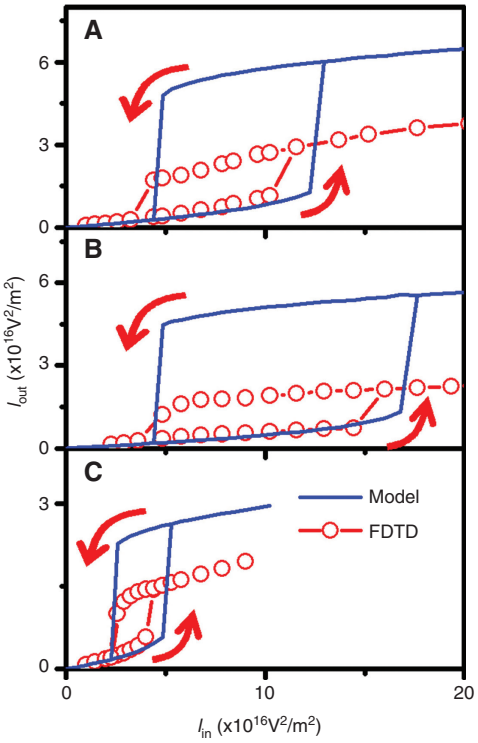

Figure 12: Bistable hysteresis.
Bistable hysteresis for a device with parameters (A) w=20 μm, h=60 μm; (B) w=20 μm, h=80 μm; (C) w=15 μm, h=60 μm, calculated by a non-linear FDTD scheme [43] (circles) and the analytic model calculations using Eqs. (12) and (14) (lines). Red arrows indicate the direction of the input power change. Reproduced from [38] with permission.

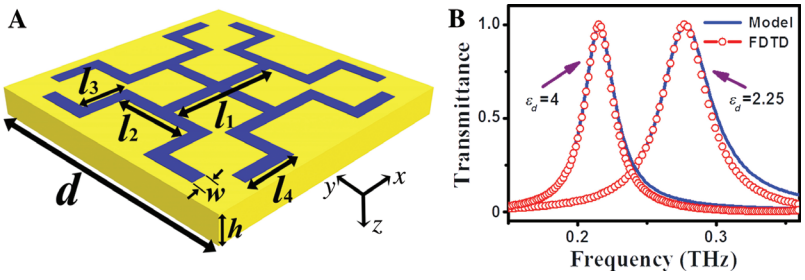

Figure 11: Schematic and transmission spectra of the device.
(A) Schematic of the device. Shown is a unit cell with d=240 mm, l_1=100 μm, l_2=l_3=40 μm, l_4=60 μm, l_4=60 μm. The yellow (blue) region denotes the metal (nonlinear material). (B) Transmission spectra of the device with varying ε_d, calculated by FDTD simulations (circles) and the analytical model (solid lines) using Eq. (12). Reproduced from [38] with permission.

(Figure 12A and B) but strongly depends on the line width w of the aperture (Figure 12A and C).

We developed an analytical model to help understand the physical mechanism. For the structure shown in Figure 11A, one can consider those subwavelength apertures (blue regions) as metallic waveguides supporting a series of eigenmodes. The wave-scattering problems related to such a structure can be rigorously solved within a general mode expansion framework [26]. Under the single-mode approximation, the linear transmittance at normal incidence is given by [46]

$$T=\left|\frac{4Y_0Y_{\text{hole}}e^{iq_zh}}{(Y_0+Y_{\text{hole}})^2-(Y_0-Y_{\text{hole}})^2e^{2iq_zh}}\right|^2, \tag{12}$$

where $Y_0=k_0/\omega\mu_0$ and $Y_{\text{hole}}=q_z/S_0^2\omega\mu_0$ are the admittances of the fundamental modes in the air and in the aperture waveguide, respectively; $q_z=k_0\sqrt{\varepsilon_d}\sqrt{1-\omega_c^2/\omega^2}$, with ω_c being the cutoff frequency of the waveguide determined by the subwavelength pattern. Meanwhile, we need to know the local field experienced by the Kerr non-linear medium. Noticing that the EM energy is stored only inside the aperture, we can estimate the average local field as

$$\left|\left\langle\vec{E}_{\text{fractal}}\right\rangle\right|^2\approx\frac{A_{\text{u.c.}}}{A_{\text{hole}}}\frac{\left|\vec{E}_{||}^{\text{inc}}\right|^2T}{|S_0|^2}, \tag{13}$$

where $A_{\text{u.c.}}/A_{\text{hole}}$ is the area correction with $A_{\text{u.c.}}$ and A_{hole} representing the areas of a unit cell and an aperture, respectively. Therefore, the permittivity of the Kerr medium can be written as

$$\varepsilon_d=2.25+\chi^{(3)}\frac{A_{\text{u.c.}}}{A_{\text{hole}}}\frac{|\vec{E}_0|^2T}{|S_0|^2}. \tag{14}$$

Eqs. (12) and (14) together form a set of coupled non-linear equations with two unknowns (T and ε_d), which can be solved using the pictorial method developed in [35]. In Figure 12, we also plot the results according to the analytic model (solid lines), compared with the rigorous FDTD ones. The agreements are in general acceptable.

The model analysis reveals the important role of plasmonic resonances in achieving such extraordinary non-linear optical effect. It is the highly enhanced local field inside the aperture that significantly enhances the LMI so as to strongly reduce the optical bistability threshold. Meanwhile, the SPP exhibits a clear nature of lateral resonance, so that the device's functionality is basically insensitive to the film thickness. Both features are the characteristics of our plasmonic MTMs, which do not belong to a conventional FP system.

5.2 Slow-wave effect and perfect absorber

In previous parts of this review, we already showed that our plasmonic MTM can significantly enhance the LMI. Such phenomenon can be interpreted from a different viewpoint. In this subsection, we show by both FDTD simulations and experiments that our plasmonic MTMs exhibit intriguing slow-wave properties, namely they can trap light for a long time so as to remarkably enhance the LMI [38, 47]. To make the slow-wave measurements easier to perform, we add a metal plate to the back of our plasmonic system to form a sandwich structure (see Figure 13). The thicknesses of the MTM layer and the spacer are h_1 and h_2, respectively. By doing so, our system becomes totally reflective, so that we only need to care about the reflected signal.

Figure 14A depicts the measured (symbols) and calculated (line) time delays (ΔT) for microwave pulses with different central frequencies being reflected by our structure. While light pulses are directly reflected by our system at most frequencies, our experiment shows that light could penetrate inside the apertures at 5.5 GHz and stay there for a long time (~2 ns) before leaving the structure. Recalling that the total thickness of our system is only $h=h_1+h_2=4$ mm, we found that the "effective" wave speed inside our structure is $v_g=2h/\Delta T\sim c/100$ at ~5.5 GHz, indicating that the system exhibits slow-wave properties near this frequency (i.e., the SPP resonance). Most intriguingly, we found that such slow-wave effect is more significant when h_1, $h_2\to0$. In addition, the slow-wave effect is

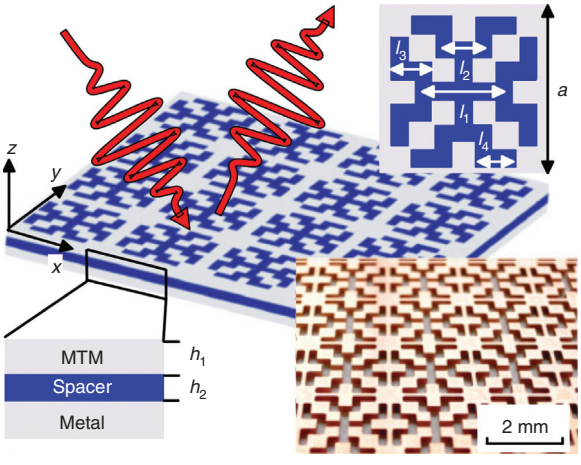

Figure 13: Geometry of the designed plasmonic MTMs and picture of part of a fabricated sample with $a=20$ mm, $w=h_1=h_2=2$ mm, $l_1=10$ mm, $l_2=l_3=l_4=5$ mm.
The metallic material used here is copper, and the spacer is just an air gap. Reproduced from [47] with permission.

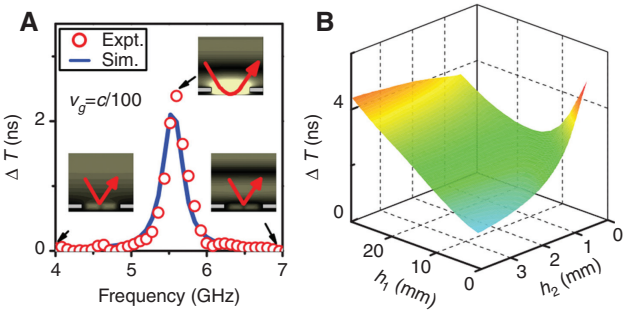

Figure 14: Delay timespectra for the MTMs.
(A) Measured (red dot) and simulated (blue lines) delay time (ΔT) spectra for the fabricated plasmonic MTMs. Insets show the calculated electric-field distributions under external radiations at different frequencies. (B) FEM-simulated delay time ΔT (calculated at frequency 5.5 GHz) as a function of h_1 and h_2 with other geometrical parameters the same as those in Figure 13. Reproduced from [47] with permission.

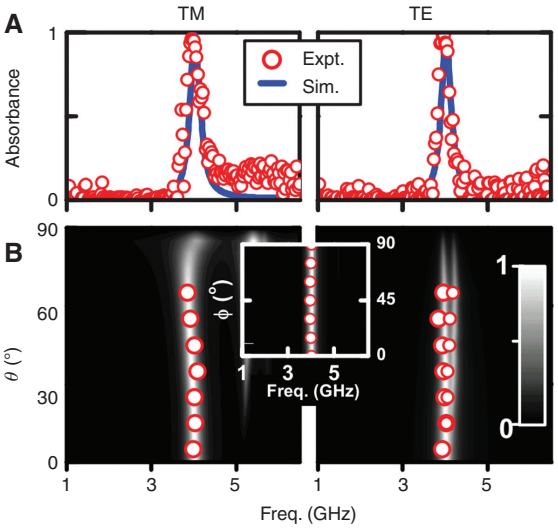

Figure 15: (A) Measured (circles) and simulated (lines) EM wave absorption spectra under radiations with TM or TE polarizations and θ=15°, φ=0°. (B) FEM-computed absorbance vs. incidence angle and frequency under radiations with TM or TE polarizations and φ=0°; circles denote the absorption peak position measured experimentally. Inset shows the measured (circles) and simulated φ-dependence of the absorption peak (setting θ=15°). Reproduced from [47] with permission.

robust against the polarization and incident angle of the input beam [47].

It is well known that LMIs will be significantly enhanced inside a slow-wave system. We take light absorption as a further example to illustrate the physics. Inserting low-absorptive FR4-PCB powders (with ε=1.5+0.03i) into the apertures and replacing the air gap by a 2-mm-thick low-absorptive dielectric spacer (with ε=3.9+0.075i), we performed microwave experiments to measure the absorption spectra of the entire system. Figure 15A shows the absorption spectra, measured with input waves taking TE or TM polarizations at an incident angle θ=15°. Absorbance is significantly enhanced in a frequency window centered at ~4 GHz with peak absorption of ~100%, and the perfect absorption effect is robust against the polarization, incident angle θ, and azimuthal angle φ of the in-plane E vector (see Figure 15B). Note that the raw materials only exhibit very weak absorption for EM wave, and such significantly enhanced absorption effect is obviously due to the slow-wave property of the system.

6 Conclusion

To summarize, we have briefly reviewed our recent works on a particular type of plasmonic MTMs – metallic plates drilled with array of deep subwavelength apertures (usually in complex fractal-like shape). We described the key physical properties (including both SPP and transmission/reflection properties) of such plasmonic MTMs, followed by an EMT description for such systems. We showed that our system at a particular frequency can well mimic the ONM – a TO medium representing optically non-existing space and thus can exhibit many interesting applications. Finally, we summarized our experimental efforts in demonstrating several potential applications of such materials, organized into two main categories, namely the imaging- and LMI enhancement-related ones. We hope that new ideas can be inspired from this review.

Acknowledgments: This work was supported by NSFC (60990321, 11174055, and 11204040), the Program of Shanghai Subject Chief Scientist (12XD1400700), and MOE of China (B06011). Q.H. acknowledges financial support from China Postdoctoral Science Foundation (2012M520039 and 2013T60412).

References

[1] Shelby RA, Smith DR, Schultz S. Experimental verification of a negative index of refraction. *Science* 2001, 292, 77–79.
[2] Pendry JB. Negative refraction makes a perfect lens. *Phys. Rev. Lett.* 2000, 85, 3966–3969.
[3] Yen TJ, Padilla WJ, Fang N, Vier DC, Smith DR, Pendry JB, Basov DN, Zhang X. Terahertz magnetic response from artificial materials. *Science* 2004, 303, 1494–1496.
[4] Linden S, Enkrich C, Wegener M, Zhou JF, Koschny T, Soukoulis CM. Magnetic response of metamaterials at 100 terahertz. *Science* 2004, 306, 1351–1353.

[5] Enkrich C, Wegener M, Linden S, Burger S, Zschiedrich L, Schmidt F, Zhou JF, Koschny T, Soukoulis CM. Magnetic metamaterials at telecommunication and visible frequencies. *Phys. Rev. Lett.* 2005, 95, 203901.
[6] Grigorenko AN, Geim AK, Gleeson HF, Zhang Y, Firsov AA, Khrushchev IY, Petrovic J. Nanofabricated media with negative permeability at visible frequencies. *Nature* 2005, 438, 335–338.
[7] Klein MW, Enkrich C, Wegener M, Soukoulis CM, Linden S. Single-slit split-ring resonators at optical frequencies: limits of size scaling. *Opt. Lett.* 2006, 31, 1259–1261.
[8] Padilla WJ, Taylor AJ, Highstrete C, Lee M, Averitt RD. Dynamical electric and magnetic metamaterial response at terahertz frequencies. *Phys. Rev. Lett.* 2006, 96, 107401.
[9] Smith DR, Schultz S, Markos P, Soukoulis CM. Determination of effective permittivity and permeability of metamaterials from reflection and transmission coefficients. *Phys. Rev. B* 2002, 65, 195104.
[10] O Brien S, McPeake D, Ramakrishna S, Pendry J. Near-infrared photonic band gaps and nonlinear effects in negative magnetic metamaterials. *Phys. Rev. B* 2004, 69, 241101.
[11] Zhou J, Koschny T, Kafesaki M, Economou EN, Pendry JB, Soukoulis CM. Saturation of the magnetic response of split-ring resonators at optical frequencies. *Phys. Rev. Lett.* 2005, 95, 223902.
[12] Pendry JB, Schurig D, Smith DR. Controlling electromagnetic fields. *Science* 2006, 312, 1780–1782.
[13] Schurig D, Mock JJ, Justice BJ, Cummer SA, Pendry JB, Starr AF, Smith DR. Metamaterial electromagnetic cloak at microwave frequencies. *Science* 2006, 314, 977–980.
[14] Zhou L, Li H, Qin Y, Wei Z, Chan CT. Directive emissions from subwavelength metamaterial-based cavities. *Appl. Phys. Lett.* 2005, 86, 101101–101103.
[15] Pendry JB, Holden AJ, Robbins DJ, Stewart WJ. Magnetism from conductors and enhanced nonlinear phenomena. *IEEE Trans. Microwave Theory Tech.* 1999, 47, 2075–2084.
[16] Ebbesen TW, Lezec HJ, Ghaemi HF, Thio T, Wolff PA. Extraordinary optical transmission through sub-wavelength hole arrays. *Nature* 1998, 391, 667–669.
[17] Garcia-Vidal FJ, Martín-Moreno L, Pendry JB. Surfaces with holes in them: new plasmonic metamaterials. *J. Opt. A Pure Appl. Opt.* 2005, 7, S97–S101.
[18] Pendry JB, Martin-Moreno L, Garcia-Vidal FJ. Mimicking surface plasmons with structured surfaces. *Science* 2004, 305, 847–848.
[19] Garcia-Vidal FJ, Martin-Moreno L, Ebbesen TW, Kuipers L. Light passing through subwavelength apertures. *Rev. Mod. Phys.* 2010, 82, 729–787.
[20] Beruete M, Sorolla M, Campillo I, Dolado JS, Martín-Moreno L, Bravo-Abad JFG. Enhanced millimeter-wave transmission through subwavelength hole arrays. *Opt. Lett.* 2004, 29, 2500–2502.
[21] Zhou L, Chan CT, Sheng P. Theoretical studies on the transmission and reflection properties of metallic planar fractals. *J. Phys. D Appl. Phys.* 2004, 37, 368–373.
[22] Wen W, Yang Z, Xu G, Chen Y, Zhou L, Ge W, Chan CT, Sheng P. Infrared passbands from fractal slit patterns on a metal plate. *Appl. Phys. Lett.* 2003, 83, 2106–2108.
[23] Huang X, Xiao S, Ye D, Huangfu J, Wang Z, Ran L, Zhou L. Fractal plasmonic metamaterials for subwavelength imaging. *Opt. Express* 2010, 18, 10377–10387.
[24] Shin Y, So J, Jang K, Won J, Srivastava A, Park G. Evanescent tunneling of an effective surface plasmon excited by convection electrons. *Phys. Rev. Lett.* 2007, 99, 147402.
[25] He Q, Xiao S, Li X, Zhou L. Optic-null medium: realization and applications. *Opt. Express* 2013, 21, 28948–28959.
[26] Xiao SY, He Q, Huang XQ, Zhou L. Super imaging with a plasmonic metamaterial: role of aperture shape. *Metamaterials* 2011, 5, 112–118.
[27] Wen W, Zhou L, Hou B, Chan C, Sheng P. Resonant transmission of microwaves through subwavelength fractal slits in a metallic plate. *Phys. Rev. B* 2005, 72, 153406.
[28] Alù A, Silveirinha MG, Salandrino A, Engheta N. Epsilon-near-zero metamaterials and electromagnetic sources: tailoring the radiation phase pattern. *Phys. Rev. B* 2007, 75, 155410.
[29] Silveirinha M, Engheta N. Tunneling of electromagnetic energy through subwavelength channels and bends using ε-near-zero materials. *Phys. Rev. Lett.* 2006, 97, 157403.
[30] Luo J, Xu P, Chen H, Hou B, Gao L, Lai Y. Realizing almost perfect bending waveguides with anisotropic epsilon-near-zero metamaterials. *Appl. Phys. Lett.* 2012, 100, 221903–221905.
[31] Khoo IC, Werner DH, Liang X, Diaz A, Weiner B. Nanosphere dispersed liquid crystals for tunable negative-zero-positive index of refraction in the optical and terahertz regimes. *Opt. Lett.* 2006, 31, 2592–2594.
[32] Litchinitser NM, Maimistov AI, Gabitov IR, Sagdeev RZ, Shalaev VM. Metamaterials: electromagnetic enhancement at zero-index transition. *Opt. Lett.* 2008, 33, 2350–2352.
[33] Kildishev AV, Narimanov EE. Impedance-matched hyperlens. *Opt. Lett.* 2007, 32, 3432–3434.
[34] Born M, Wolf E. *Principles of Optics*, 4th ed., Pergamon Press: Elmsford, NY, 1970.
[35] Felber FS, Marburger JH. Theory of nonresonant multistable optical devices. *Appl. Phys. Lett.* 1976, 28, 731–733.
[36] Marburger JH, Felber FS. Theory of a lossless nonlinear Fabry-Perot interferometer. *Phys. Rev. A* 1978, 17, 335–342.
[37] Chen W, Mills DL. Optical response of a nonlinear dielectric film. *Phys. Rev. B* 1987, 35, 524.
[38] Tang SW, Zhu BC, Xiao SY, Shen J, Zhou L. Low-threshold optical bistabilities in ultrathin nonlinear metamaterials. *Opt. Lett.* 2014, 39, 3212–3215.
[39] Khanikaev AB, Mousavi SH, Shvets G, Kivshar YS. One-way extraordinary optical transmission and nonreciprocal spoof plasmons. *Phys. Rev. Lett.* 2010, 105, 126804.
[40] Yu NF, Wang QJ, Kats MA, Fan JA, Khanna SP, Li L, Davies AG, Linfield EH, Capasso F. Designer spoof surface plasmon structures collimate terahertz laser beams. *Nat. Mater.* 2010, 9, 730–735.
[41] Ueba Y, Takahara J, Nagatsuma T. Thermal radiation control in the terahertz region using the spoof surface plasmon mode. *Opt. Lett.* 2011, 36, 909–911.
[42] Martin-Cano D, Quevedo-Teruel O, Moreno E, Martin-Moreno L, Garcia-Vidal FJ. Waveguided spoof surface plasmons with deep-subwavelength lateral confinement. *Opt. Lett.* 2011, 36, 4635–4637.
[43] *EastFDTD V4.0*, Dongjun Science and Technology Co., China.
[44] Mayer A, Keilmann F. Far-infrared nonlinear optics. II: X(3) contributions from the dynamics of free carriers in semiconductors. *Phys. Rev. B* 1986, 33, 6962–6968.

[45] Brazis R, Raguotis R, Siegrist MR. Suitability of drift nonlinearity in Si, GaAs, and InP for high-power frequency converters with a 1 THz radiation output. *J. Appl. Phys.* 1998, 104, 3474–3482.
[46] Jung J, García-Vidal F, Martín-Moreno L, Pendry J. Holey metal films make perfect endoscopes. *Phys. Rev. B* 2009, 79, 153407.
[47] Xiao S, He Q, Huang X, Tang S, Zhou L. Enhancement of light-matter interactions in slow-wave metasurfaces. *Phys. Rev. B* 2012, 85, 85125.

Bionotes

Shiwei Tang
State Key Laboratory of Surface Physics and Key Laboratory of Micro and Nano Photonic Structures (Ministry of Education), Fudan University, Shanghai 200433, China

Shiwei Tang received his BS degree in applied physics from the Northwestern Polytechnical University (Xi'an, China) in 2008 and his PhD degree in theoretical physics from Fudan University (Shanghai, China) in 2014. He is currently a postdoctoral fellow at Materials Science Department of Fudan University. His current research interests focus on metamaterials, plasmonics, and nanomembranes.

Qiong He
State Key Laboratory of Surface Physics and Key Laboratory of Micro and Nano Photonic Structures (Ministry of Education), Fudan University, Shanghai 200433, China

Qiong He received his PhD degree from Paris-Sud University (Orsay, France) in 2008. He is currently a lecturer at the Physics Department of Fudan University (Shanghai, China). His research interests focus on metamaterial and plasmonics.

Shiyi Xiao
State Key Laboratory of Surface Physics and Key Laboratory of Micro and Nano Photonic Structures (Ministry of Education), Fudan University, Shanghai 200433, China

Shiyi Xiao received his BS degree in applied physics from Tongji University (Shanghai, China) in 2007 and his PhD degree in physics from Fudan University (Shanghai, China) in 2013. He is currently working at the University of Birmingham as a research fellow.

Xueqin Huang
State Key Laboratory of Surface Physics and Key Laboratory of Micro and Nano Photonic Structures (Ministry of Education), Fudan University, Shanghai 200433, China

Xueqin Huang received his PhD in physics from Fudan University (Shanghai, China) in 2009. He is currently a postdoctoral fellow at Hong Kong University of Science and Technology. His current research interests focus on photonic crystal, metamaterial, and plasmonics.

Lei Zhou
State Key Laboratory of Surface Physics and Key Laboratory of Micro and Nano Photonic Structures (Ministry of Education), Fudan University, Shanghai 200433, China, **phzhou@fudan.edu.cn**

Lei Zhou is a professor of physics at Fudan University (Shanghai, China). He received his BS degree in physics and his PhD degree in theoretical physics from Fudan University. In 1997, he went to the Institute for Material Research, Tohoku University, Japan, for postdoctoral research. He left Japan for Hong Kong in 2000 and became a visiting scholar in the Physics Department of Hong Kong University of Science and Technology. In 2004, he joined the Physics Department of Fudan University as a professor. His current research interests focus on metamaterials, plasmonics, and photonic crystals.